Multiple incommensurate magnetic states in the kagome antiferromagnet $Na_2Mn_3Cl_8$

Joseph A. M. Paddison [1,*] Li Yin,[1] Keith M. Taddei,[2] Malcolm J. Cochran,[2] Stuart Calder [2] David S. Parker,[1] and Andrew F. May [1,†]

[1]*Materials Science and Technology Division, Oak Ridge National Laboratory, Oak Ridge, Tennessee 37831, USA*
[2]*Neutron Scattering Division, Oak Ridge National Laboratory, Oak Ridge, Tennessee 37831, USA*

(Received 17 April 2023; revised 11 July 2023; accepted 21 July 2023; published 16 August 2023)

The kagome lattice can host exotic magnetic phases arising from frustrated and competing magnetic interactions. However, relatively few insulating kagome materials exhibit incommensurate magnetic ordering. Here, we present a study of the magnetic structures and interactions of antiferromagnetic $Na_2Mn_3Cl_8$ with an undistorted Mn^{2+} kagome network. Using neutron-diffraction and bulk magnetic measurements, we show that $Na_2Mn_3Cl_8$ hosts two different incommensurate magnetic states, which develop at $T_{N1} = 1.6$ K and $T_{N2} = 0.6$ K. Magnetic Rietveld refinements indicate magnetic propagation vectors of the form $\mathbf{q} = (q_x, q_y, \frac{3}{2})$, and our neutron-diffraction data can be well described by cycloidal magnetic structures. By optimizing exchange parameters against magnetic diffuse-scattering data, we show that the spin Hamiltonian contains ferromagnetic nearest-neighbor and antiferromagnetic third-neighbor Heisenberg interactions, with a significant contribution from long-ranged dipolar coupling. This experimentally determined interaction model is compared with density-functional-theory simulations. Using classical Monte Carlo simulations, we show that these competing interactions explain the experimental observation of multiple incommensurate magnetic phases and may stabilize multi-**q** states. Our results expand the known range of magnetic behavior on the kagome lattice.

DOI: 10.1103/PhysRevB.108.054423

I. INTRODUCTION

Geometrical frustration—the inability of a system to satisfy all of its pairwise interactions simultaneously—can suppress conventional magnetic ordering and promote exotic magnetic states [1]. A focus of frustrated-magnetism research has been insulating materials in which magnetic ions occupy a kagome lattice of corner-sharing triangles, where strong frustration effects can occur if the interactions are antiferromagnetic. For example, if antiferromagnetic Heisenberg interactions couple neighboring spins only, a spin-liquid state is stable down to extremely low temperatures even in the classical limit [2], before eventually undergoing octupolar magnetic ordering [3]. There is a continuing search for real materials that are candidates to realize frustrated kagome magnetism [4]. In the quantum ($S = 1/2$) limit, notable candidates include herbertsmithite [5,6] and barlowite [7–9]. In the classical (large-S) limit, probably the most studied candidates are iron-containing jarosite minerals [10–12], which are often off-stoichiometric [13,14]. Therefore, an important goal is to identify and characterize other structure types containing kagome lattices, particularly those with antiferromagnetic interactions, and where the kagome lattice is structurally undistorted.

Kagome antiferromagnets that exhibit long-range magnetic ordering may still show strong effects of geometrical frustration. In particular, the inclusion of further-neighbor interactions can stabilize several unusual magnetic states instead of conventional collinear antiferromagnetism. These states include noncollinear 120° order as well as many noncoplanar states, which are more stable than collinear antiferromagnets in large regions of interaction space [15]. For certain exchange interactions, incommensurate magnetic ordering can also be stabilized; however, the nature of the incommensurate phase is difficult to determine from simulations [16,17]. Experimental studies of materials that occupy this part of the interaction space are therefore important to advance our understanding of kagome magnetism.

In this context, we identified $Na_2Mn_3Cl_8$ as a promising material for frustrated magnetism on the kagome lattice. This material was first reported in the 1970s [18] and is likely electrically insulating [19], but its magnetic structure and interactions have not previously been studied. Nevertheless, a recent materials survey highlighted $Na_2Mn_3Cl_8$ as a candidate frustrated antiferromagnet [20]. Due to the large magnetic moment of Mn^{2+} with $S = 5/2$ and the absence of an orbital contribution ($L = 0$), its behavior is expected to be predominantly classical. The reported crystal structure [18] is shown in Fig. 1(a); its trigonal symmetry (space group $R\bar{3}m$) with Mn at the $3b$ Wyckoff position ensures that the kagome planes are undistorted. A recent investigation of its bulk magnetic properties showed multiple magnetic phase transitions below 2 K, and the possibility of a low-temperature structural phase transition was suggested due to the observation of a broad specific-heat anomaly around 6 K [19]. Notably, a structural transition to a trimerized polar phase is observed in the related $S = 1$ kagome magnet $Na_2Ti_3Cl_8$ [21–25].

*paddisonja@ornl.gov
†mayaf@ornl.gov

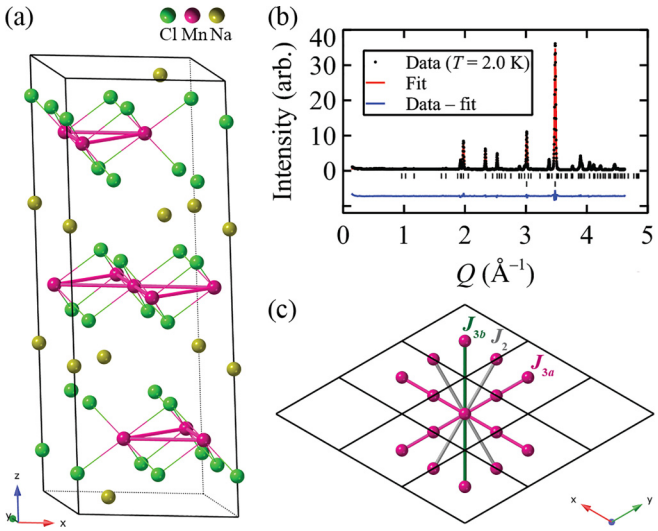

FIG. 1. (a) Crystal structure of $Na_2Mn_3Cl_8$, showing Mn^{2+} (magenta), Cl^-(green), and Na^+(yellow) ions. (b) Neutron powder diffraction data collected at $T = 2$ K (black circles), fitted curve from Rietveld refinement (red line), and data fit (blue line). Experimental data were collected using the HB-2A diffractometer at ORNL ($\lambda = 2.4109$ Å). The upper and lower tick marks indicate the positions of nuclear Bragg peaks from $Na_2Mn_3Cl_8$ and the Cu sample container, respectively. (c) Magnetic interaction pathways within the kagome Mn^{2+} layers, showing next-nearest neighbor interactions J_2 and the two distinct third-neighbor interactions, J_{3a} and J_{3b}. The nearest-neighbor interaction pathway is parallel to J_{3a} at one half of its distance.

In this paper, we report magnetic characterization and powder neutron-diffraction experiments on $Na_2Mn_3Cl_8$. In agreement with a recent report [19], we observe that this material undergoes two magnetic phase transitions with decreasing temperature. However, our data do not indicate a measurable crystallographic distortion at temperatures down to 0.3 K, indicating that the undistorted kagome lattice is preserved. Our powder neutron-diffraction measurements show that, unusually, the two ordered magnetic states both have incommensurate magnetic propagation vectors. These data are consistent with single-**q** helical magnetic ordering, with an antiferromagnetic stacking of kagome layers. We show that the development of multiple incommensurate phases can be explained by a model including Heisenberg exchange interactions up to third-nearest neighbors and the long-ranged dipolar interaction, and we estimate the values of the exchange interactions by analyzing the magnetic diffuse scattering measured above T_{N1}. Our results place $Na_2Mn_3Cl_8$ in a complex region of the kagome phase space, in which incommensurate ordering is stabilized by a competition between short-range ferromagnetic and longer-range antiferromagnetic interactions. Our interaction model also suggests that $Na_2Mn_3Cl_8$ deserves further investigation as a potential host of multi-**q** spin textures in zero applied magnetic field.

Our paper is structured as follows. We first introduce the crystal structure and potential magnetic exchange pathways of $Na_2Mn_3Cl_8$, and present thermomagnetic measurements of the bulk magnetic properties. We then discuss our powder neutron-diffraction data and symmetry-informed Rietveld analysis, from which the likely single-**q** magnetic structures are determined. Magnetic diffuse-scattering analysis is employed to parametrize the magnetic interactions that stabilize incommensurate ordering. We compare and contrast our experimental results with density-functional-theory calculations. Finally, we discuss the extent to which our experimental observations can be rationalized using field-theoretical and Monte Carlo simulations and conclude by summarizing our results and highlighting opportunities for future research.

II. METHODS

A. Sample synthesis

A polycrystalline sample (mass 2.1 g) of $Na_2Mn_3Cl_8$ was prepared by sealing a stoichiometric mixture $MnCl_2$ and NaCl in SiO_2 after heating at 250 °C under dynamic vacuum overnight. The mixture was heated to 750 °C for several hours and quenched by removing from the furnace. The sample was ground, sealed with $\frac{1}{4}$-atm argon, and annealed at 350 °C for at total of ≈260 h with an additional intermediate grinding. All handling of this very air-sensitive sample was conducted in an inert-atmosphere glovebox, and the samples were kept under inert atmosphere when they were transferred to the vacuum lines for sealing of the silica tubes.

B. Experimental measurements

Magnetization measurements were performed using Quantum Design magnetometers with data below 1.8 K collected using a ^{3}He insert. The samples were loaded into measurement straws in an inert-atmosphere glovebox with grease to protect the powders from air during the rapid loading process. Specific heat data were collected at temperatures down to 0.4 K using a ^{3}He insert.

Neutron-diffraction measurements were performed using the HB-2A powder diffractometer at the High Flux Isotope Reactor of Oak Ridge National Laboratory. The incident neutron wavelength $\lambda = 2.4109$ Å. Our powder sample of mass 2.1 g was loaded into a 4-mm-diameter cylindrical Cu container in a He glovebox. The sample was cooled using a dry ^{3}He cryostat, affording a base temperature of ≈0.3 K. Counting times were ≈3 hr at 0.3, 0.8, 2.0, 5.0, and 40 K, and ≈0.5 hr at other temperatures below T_{N1}. The data were corrected for neutron absorption by the sample [26].

C. Magnetic diffuse scattering refinements and field theory

Magnetic diffuse-scattering refinements were performed using the SPINTERACT program to refine the values of the exchange interactions [27]. The spin Hamiltonian included Heisenberg exchange interactions and the magnetic dipolar interaction (see Sec. III E). The input data were collected at 2 and 5 K and were placed in absolute intensity units (barn sr^{-1} Mn^{-1}) by normalization to the nuclear Bragg profile. A high-temperature (40 K) data set was subtracted from these data.

The magnetic diffuse scattering $I(Q)$ and bulk susceptibility χT were calculated using Onsager reaction-field theory [27–29], and a 40 K calculation was subtracted from the calculated $I(Q)$. In this approach, the Fourier

TABLE I. Refined crystallographic parameters of $Na_2Mn_3Cl_8$ at $T = 2$ K, obtained from Rietveld refinement to powder neutron-diffraction data ($\lambda = 2.4109$ Å).

$Na_2Mn_3Cl_8$, $T = 2$ K $R\bar{3}m$, $a = 7.4249(1)$ Å, $c = 19.4971(4)$ Å $B_{\text{overall}} = 0.31(6)$ Å^2		
Site	Wyckoff	(x, y, z)
Na	6*c*	(0,0,0.3395(7))
Mn	3*b*	$(0, 0, \frac{1}{2})$
Cl1	6*c*	(0,0,0.9062(4))
Cl2	18*h*	(0.5081(3),0.4919(3),0.0931(2))

transform of the magnetic interactions is calculated as $J_{ij}^{\alpha\beta}(\mathbf{q}) = \sum_{\mathbf{r}} J_{ij}^{\alpha\beta}(\mathbf{r}) \exp(-i\mathbf{q}\cdot\mathbf{r})$, where α, β denote Cartesian spin components, $i, j \in \{1, 3\}$ denote sites within the primitive unit cell, and $\mathbf{r}$ is the vector connecting unit cells containing sites i and j. The interaction matrix formed by the $J_{ij}^{\alpha\beta}(\mathbf{q})$ is diagonalized on a grid of up to 50^3 points in the first Brillouin zone to determine its eigenvalues $\lambda_\mu(\mathbf{q})$ and eigenvector components $U_{i\mu}^{\alpha}(\mathbf{q})$,

$$\lambda_\mu(\mathbf{q}) U_{i\mu}^{\alpha}(\mathbf{q}) = \sum_j J_{ij}^{\alpha\beta}(\mathbf{q}) U_{j\mu}^{\beta}(\mathbf{q}),$$

where $\mu \in \{1, 3\}$ indexes the normal modes. The long-range dipolar interaction is included using Ewald summation [30]. Within a reciprocal-space mean-field approximation, the magnetic propagation vector of the first ordered state is the wave vector at which λ_μ reaches its maximal value. The $I(Q)$ and χT are given in terms of the $\lambda_\mu(\mathbf{q})$ and $U_{i\mu}^{\alpha}(\mathbf{q})$, as described in Ref. [27].

During the refinements, we minimized the function

$$\chi^2 = \sum_i \left(\frac{I_{\text{expt}}^i - s I_{\text{calc}}^i}{\sigma_i} \right)^2, \quad (1)$$

where subscript "expt" and "calc" indicate measured and calculated diffuse scattering patterns, respectively, σ is an experimental uncertainty, and s is a refined overall scale factor common to the neutron-scattering data and the magnetic susceptibility χT. The minimization was performed using the MINUIT program [31,32]. To identify local minima in χ^2, we performed 25 refinements for each model, with different randomly chosen initial parameter values in each case.

D. Rietveld refinements

Rietveld refinements were performed using the FULLPROF software [33,34]. A crystal-structure refinement was first performed at $T = 2$ K ($> T_{N1}$). In addition to the crystallographic parameters given in Table I, we refined the intensity scale factor, 2θ zero-offset, peak-shape, and background parameters. The peak shape was modeled using a pseudo-Voigt function initialized with the instrument resolution parameters, with U, V, and W parameters subsequently refined. The background was fitted using Chebychev polynomials.

Magnetic Rietveld refinements were performed against 0.3 K and 0.8 K data from which the 2 K data had been subtracted. This subtraction isolates the magnetic Bragg signal by subtracting the nuclear and background contributions, which are essentially unchanged between 0.3 and 2 K. In the magnetic refinements, asymmetry, Chebychev background, and magnetic-structure parameters were refined, as described in Sec. III D; all other parameters were fixed at the values obtained from the 2 K refinement. Magnetic-structure figures were prepared using the VESTA program [35].

E. Density-functional-theory calculations

Density functional theory calculations were performed using the all-electron-density functional code WIEN2K [36,37]. The linearized augmented plane wave method [38] and the generalized-gradient approximation of Perdew, Burke, and Ernzerhof [39] were utilized. The $RK_{\max}$ generated by the smallest linearized augmented plane wave sphere radius (R) and the interstitial plane-wave cutoff ($K_{\max}$) was set as 7.0 for good convergence. The muffin-tin radii of Na, Cl, and Mn atoms were 2.47, 2.14, and 2.49 a.u., respectively. The number of $\mathbf{q}$-points in the full Brillouin zone was 200. Lattice parameters of $Na_2Mn_3Cl_8$ were fixed to the experimental values of $a = b = 7.423$ Å and $c = 19.497$ Å. Then, the internal atomic coordinates were relaxed until forces on all of the atoms were less than 1 mRy/bohr, with nonmagnetic, ferromagnetic [FM, $\mathbf{q} = (0, 0, 0)$], and interlayer antiferromagnetic [interlayer-AFM, $\mathbf{q} = (0, 0, \frac{3}{2})$] states. The relaxed crystal structure with a FM state is highly similar to the experimental crystal structure. However, in the nonmagnetic state, the atomic coordination changes significantly, as Cl atoms moves towards the Mn layers. The relaxed interlayer-AFM crystal structure is same as the FM crystal structure, but exhibits lower energy and smaller forces, due solely to the different magnetic ordering. The energy difference between FM and interlayer-AFM states is 1.19 meV/f.u..

To estimate the net energetic effect of neglecting spin-orbit coupling (SOC), we conducted calculations of the FM and interlayer-AFM states with SOC and magnetization along the trigonal axis. We find this energy difference to be essentially equal (1.17 meV/f.u.) to the original energy difference without SOC, suggesting that SOC is negligible in this material.

To calculate the interlayer and intralayer interactions illustrated in Fig. 1(c), we built several supercells with different magnetic orders, as shown in Fig. 2. Our approach is similar to that of Refs. [40–42]. The $1\times1\times2$ supercell in Fig. 2(a) is built for calculating the interlayer interaction J_c. The $1\times1\times1$ supercell in Fig. 2(b) displays the J_1, J_2, and J_c interactions. The $1\times2\times1$ supercell in Fig. 2(c) and $2\times1\times1$ supercells in Figs. 2(d) and 2(e) contain the magnetic orders with J_1, J_2, J_{3a}, J_{3b}, and J_c interactions. Employing these five supercells and the $1\times1\times1$ supercell with ferromagnetic order, we calculated the interactions listed in Table IV.

III. EXPERIMENTAL RESULTS

A. Crystal structure refinement

The crystal structure of $Na_2Mn_3Cl_8$ is shown in Fig. 1(a), and comprises of triangular Na^+ layers separating kagome Mn^{2+} layers [18,19]. We performed Rietveld refinements against our 2 K and 40 K neutron-diffraction data to investigate the possibility of a crystallographic distortion from

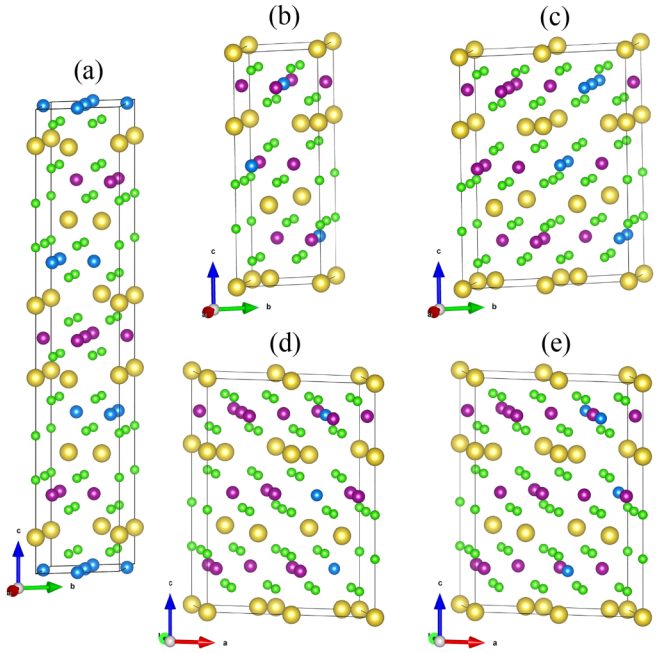

FIG. 2. The (a) 1×1×2, (b) 1×1×1, (c) 1×2×1, and (d), (e) 2×1×1 supercells with different magnetic orders for calculating the intralayer and interlayer interactions. The yellow and green balls represent the Na and Cl atoms. The purple and blue balls denote the spin-up and spin-down Mn atoms.

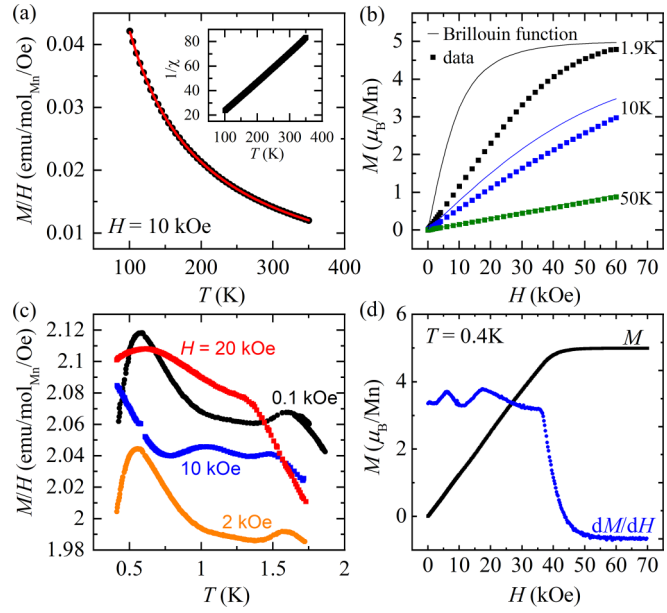

FIG. 3. Overview of bulk magnetic measurements. (a) High-temperature powder magnetic susceptibility $\chi \approx M/H$ measured in applied field of 10 kOe (black squares), and Curie-Weiss fit (red line). (b) Dependence of magnetization M on applied field H at temperatures of 1.9, 10, and 50 K (black, blue, and green squares, respectively). (c) Low-temperature magnetic susceptibility measured in applied fields of 0.1 (black points), 2 (orange points), 10 (blue points), and 20 kOe (red points). The 0.1 kOe data indicate magnetic phase transitions at approximately 0.6 and 1.6 K. (d) Dependence of magnetization M on applied field H at 0.4 K (black squares) and its field derivative (blue circles).

the published structure (space group $R\bar{3}m$) [Fig. 1(b)]. Good agreement was obtained with the published structural model [18] at both temperatures, except for two very weak peaks at 1.64 and 2.16 Å^{-1} that were not accounted for, and were unchanged between 0.3 and 40 K. Since these peaks could not be explained by simple multiples of the crystallographic unit cell, or by possible impurity phases (NaCl, $MnCl_2$, or $NaMnCl_3$), we concluded that the sample or its environment contained a small fraction of unknown impurity. Our results do not show evidence for any structural phase transition between 2 and 40 K, indicating that the broad ∼6 K specific-heat anomaly reported previously [19] is probably due to magnetic ordering of a minor $NaMnCl_3$ impurity phase (a possibility noted in Ref. [19]).

Each nearest-neighbor Mn–Mn bond is bridged by a Cl1 ion and a Cl2 ion, which provide the nearest-neighbor superexchange pathways. The Mn–Cl1–Mn and Mn–Cl2–Mn bond angles are 92.42° and 94.03°, respectively. Since these values are close to 90°, the Goodenough-Kanamori rules predict weak ferromagnetic nearest-neighbor exchange interactions. Further-neighbor interactions have more complicated pathways and, consequently, are difficult to predict. In particular, there are two inequivalent third-neighbor exchange pathways with the same interatomic separation [Fig. 1(c)].

B. Thermomagnetic measurements

Our high-temperature bulk magnetic susceptibility measurements and Curie-Weiss fits are shown in Fig. 3(a). They reveal an effective magnetic moment of 5.99 μ_B, close to the spin-only value of 5.92 μ_B for Mn^{2+}, and a Weiss temperature of $\theta_W = -4.6(1)$ K, indicating net antiferromagnetic interactions. Figure 3(b) shows the magnetic-field dependence of the magnetization, which does not follow the Brillouin function at low temperatures ($\lesssim 10$ K), in qualitative agreement for theoretical predictions for the kagome lattice [43].

An anomaly is observed at $T_{N1} \approx 1.6$ K in our low-temperature magnetic susceptibility data measured in a small applied field of 0.1 kOe. This anomaly is suppressed to lower temperature with increasing applied field, consistent with a magnetic ordering transition [Fig. 3(c)]. The "frustration parameter", $f = \theta_W/T_{N1} \approx 3$, indicates a relatively small degree of frustration. Since the nearest-neighbor kagome antiferromagnet is highly frustrated, this result hints at the presence of significant further-neighbor couplings or anisotropies; however, the nature of these couplings cannot be determined from bulk characterization data alone. Interestingly, and consistent with Ref. [19], we also observe a second magnetic-susceptibility anomaly at $T_{N2} \approx 0.6$ K [Fig. 3(c)], suggesting a multi-stage magnetic ordering process. Such behavior is unusual and hints that, despite the relatively small value of f, the frustrated topology of the kagome lattice may cause several magnetic structures to be nearly degenerate. Figure 3(d) shows the field derivative of the magnetization, dM/dH, in the magnetically ordered phase below T_{N2}. Several anomalies are observed in dM/dH at small applied fields, suggesting that the magnetic ground state is fragile to external perturbations. The fine features in dM/dH observed in Fig. 3(d) were also verified by ac susceptibility measurements as a function

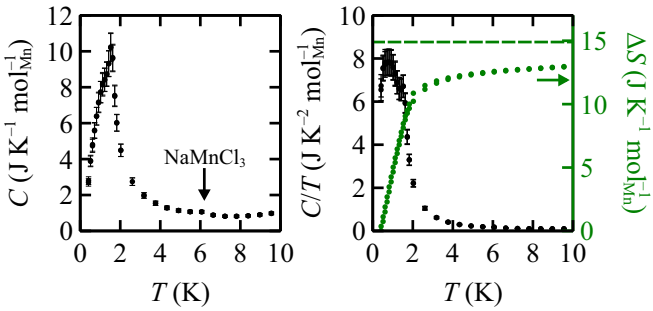

FIG. 4. (a) Heat capacity of $Na_2Mn_3Cl_8$, showing an anomaly at 1.6 K and a shoulder at ∼0.6 K. (b) Heat capacity divided by temperature, C/T (black circles, left axis) and magnetic entropy change $\Delta S(T_{\max})$ obtained by integrating C/T from 0.4 K to $T_{\max}$ (green circles, right axis). The expected magnetic entropy change of $R\ln(2S+1)$ is indicated by a green dashed line in (b).

of dc field, which effectively probes the local dM/dH. Similar behaviors were observed in the ac and dc measurements.

Specific-heat data are shown in Fig. 4(a). An anomaly is observed at 1.6 K and a shoulder at ∼0.6 K, consistent with the transition temperatures observed in magnetometry and with Ref. [19]. We observe a weak additional peak near 6.2 K, but its magnitude is much smaller than reported in Ref. [19], suggesting that it originates from magnetic ordering of a small amount of $NaMnCl_3$ impurity. Fig. 4(b) shows the heat capacity divided by temperature, C/T, and the magnetic entropy change $\Delta S(T_{\max})$ obtained by integrating C/T from 0.4 K to $T_{\max}$. Data for a phonon background are not available but the phonon ($\propto T^3$) contribution to C/T is evidently very small below $T \lesssim 10$ K. For $T_{\max} = 10$ K, the magnetic entropy change reaches approximately 87% of the expected magnetic entropy of $R\ln(2S+1)$ per Mn; the shortfall is likely due to the absence of data below 0.4 K.

C. Overview of neutron data

We performed neutron-diffraction measurements to obtain microscopic insight into the magnetic interactions and structures of $Na_2Mn_3Cl_8$ (see Methods). An overview of the temperature dependence of our neutron data is shown in Fig. 5. Several new Bragg peaks appear below $T_{N1} \approx 1.6$ K, most prominently at wave vectors of approximately 0.6 and 1.5 Å^{-1}. We identify these as magnetic Bragg peaks arising from the onset of long-range magnetic ordering, since they appear at the same temperature as the magnetic-susceptibility anomaly at T_{N1}. Interestingly, the positions of the magnetic Bragg peaks suddenly shift at $T_{N2} \approx 0.6$ K, revealing that the second phase transition involves a change in magnetic propagation vector. At temperatures above T_{N1}, broad magnetic diffuse scattering features can be seen, indicating the development of short-range magnetic correlations as T_{N1} is approached from above. We discuss the Bragg and diffuse magnetic scattering in Secs. III D and III E, respectively.

D. Magnetic structures from Rietveld refinements

We first discuss possible ordered magnetic structures of $Na_2Mn_3Cl_8$, as determined by analyzing the magnetic Bragg profiles obtained at temperatures below T_{N1}.

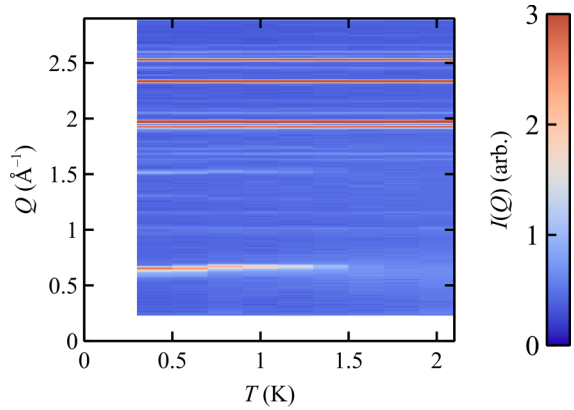

FIG. 5. Overview of neutron-diffraction data, showing diffraction intensity in false color as a function of temperature T and wave vector Q. Magnetic ordering at $T_{N1} \approx 1.6$ K is indicated by the appearance of new (magnetic) Bragg peaks, and the magnetic phase transition at $T_{N2} \approx 0.6$ K is indicated by a change in position of these peaks. Nuclear peaks, such as the four intense peaks at $Q > 1.8$ Å^{-1}, do not change position with temperature.

We used the program KSEARCH of the FULLPROF suite [33,34] to identify possible propagation vectors at 0.3 K ($T < T_{N2}$) and 0.8 K ($T_{N2} < T < T_{N1}$). The positions of 10 magnetic peaks (at 0.8 K) and 15 magnetic peaks (at 0.3 K) were provided as input, and a systematic search of candidate propagation vectors $\mathbf{q} = q_x\mathbf{a}^* + q_y\mathbf{b}^* + q_z\mathbf{c}^*$ was performed, starting with those that lie on a symmetry point, line, or plane of the Brillouin zone. However, none of the high-symmetry propagation vectors was compatible with the observed Bragg positions, at either temperature. The best-fit propagation vectors were instead of the form $(q+\delta, q-\delta, \frac{3}{2})$, with $\delta \ll q$. We obtain $(q,\delta) \approx (0.29, 0.02)$ at 0.8 K and $(q,\delta) \approx (0.27, 0.06)$ at 0.3 K; precise values are given in Table II.

TABLE II. Refined values of magnetic-structure parameters for different single-$\mathbf{q}$ models, and corresponding goodness-of-fit metric $R_{\rm wp}$. The refined parameters are defined in the text.

$Na_2Mn_3Cl_8$, magnetic
$\mathbf{q} = (0.3282(3), 0.2117(3), \frac{3}{2})$ at $T = 0.3$ K
$\mathbf{q} = (0.3102(4), 0.2646(4), \frac{3}{2})$ at $T = 0.8$ K

T (K)	Structure	$\mu_{\mathbf{q}\parallel}$ (μ_B)	$\mu_{\mathbf{q}\perp}$ (μ_B)	$\mu_{\mathbf{c}}$ (μ_B)	$R_{\rm wp}$ (%)
0.3	sine	1.15(16)	6.02(4)	−0.48(22)	25.7
0.8	sine	0.25(18)	5.32(4)	−0.86(21)	30.5
T (K)	Structure	$\mu_{\rm ord}$ (μ_B)	$\Delta\phi$ (°)	θ (°)	$R_{\rm wp}$ (%)
0.3	$\mathbf{q}_\parallel\mathbf{c}$ helix	5.35(6)	0*	0*	37.9
	$\mathbf{q}_\perp\mathbf{c}$ helix	4.85(5)	0*	0*	29.3
	ab helix	4.77(5)	0*	0*	28.2
	ab helix	4.55(5)	22(2)	0*	27.9
	helix	4.84(6)	0*	≈35	27.5
0.8	$\mathbf{q}_\parallel\mathbf{c}$ helix	4.66(6)	0*	0*	41.5
	$\mathbf{q}_\perp\mathbf{c}$ helix	4.20(5)	0*	0*	33.0
	ab helix	4.23(5)	0*	0*	31.9
	ab helix	4.06(5)	91(3)	0*	30.0
	helix	4.23(5)	0*	$\lesssim 30$	31.9

These propagation vectors lie on a general position, but they are close to the high-symmetry $(q, q, \frac{3}{2})$ plane.

Having determined possible propagation vectors, we used the program SARAH [44] to identify symmetry-allowed magnetic structures. The primitive unit cell contains three Mn^{2+} sites, with fractional coordinates $\mathbf{r}_1 = (\frac{1}{2}, 0, \frac{1}{2})$, $\mathbf{r}_2 = (0, \frac{1}{2}, \frac{1}{2})$, and $\mathbf{r}_3 = (\frac{1}{2}, \frac{1}{2}, \frac{1}{2})$ with respect to the conventional axes **a**, **b**, **c**. Each site has three magnetic degrees of freedom, which are not further constrained by symmetry. We choose these as basis-vector components along orthonormal axes $\mathbf{q}_\parallel$, $\mathbf{q}_\perp$, $\hat{\mathbf{c}}$, where $\hat{\mathbf{c}}$ is parallel to the c-axis, $\mathbf{q}_\parallel$ is parallel to the projection of $\mathbf{q}$ in the ab-plane, and $\mathbf{q}_\perp = \hat{\mathbf{c}} \times \mathbf{q}_\parallel$ is perpendicular to $\mathbf{q}_\parallel$ and **c**. These structures are amplitude-modulated spin-density waves (sine structures), with different spin magnitudes and orientations for each site,

$$\mu^j_{\text{sine}}(\mathbf{R}) \propto \left(\mu^j_{\mathbf{q}_\parallel}, \mu^j_{\mathbf{q}_\perp}, \mu^j_{\mathbf{c}}\right) \exp(-2\pi i \mathbf{q} \cdot \mathbf{R}) + \text{c.c.}, \qquad (2)$$

where $\mathbf{q}$ denotes the propagation vector, $\mathbf{R}$ denotes a lattice vector, $j \in \{1, 3\}$ labels sites within the unit cell, and $\mu_{\mathbf{q}_\parallel}, \mu_{\mathbf{q}_\perp}, \mu_{\mathbf{c}}$ are basis-vector components. Alternatively, it is possible to construct helical structures such as

$$\mu^j_{\text{helix}}(\mathbf{R}) \propto \left(\mu^j_{\mathbf{q}_\parallel}, i\mu^j_{\mathbf{q}_\perp}, 0\right) \exp(-2\pi i \mathbf{q} \cdot \mathbf{R}) + \text{c.c.}, \qquad (3)$$

where, in this case, the spin plane is perpendicular to the c-axis. The ordered magnetic-moment length can be identical on all sites in the crystal in a helical structure, for example if $\mu_{\mathbf{q}_\parallel} = \mu_{\mathbf{q}_\perp}$ in Eq. (3).

Due to the relatively large number of variable parameters and the limitations of powder data, we make two assumptions when testing candidate magnetic structures. First, we only consider structures that order with a single propagation vector (single-**q** structures). While multi-**q** structures are possible, they cannot generally be distinguished from single-**q** structures by powder diffraction [45]. Second, we initially assume that the basis vectors at sites $\mathbf{r}_1$, $\mathbf{r}_2$, and $\mathbf{r}_3$ are parallel; this assumption is reasonable because the interactions between nearest and next-nearest neighbors are ferromagnetic, as we will show in Sec. III E. Magnetic-structure models were tested against the magnetic Bragg profile using Rietveld refinement (see Methods). We first considered amplitude-modulated sine structures. The assumption of parallel basis vectors reduces the number of refined parameters from 9 to 3. Sine structures yield excellent agreement with our data at both 0.3 and 0.8 K, as shown in Figs. 6(a) and 6(e), respectively. The magnetic moment is predominantly oriented along $\mathbf{q}_\perp$ for the corresponding structures, which are shown in Figs. 6(c) and 6(g), respectively. The refined parameter values and goodness-of-fit metric R_{wp} are given in Table II. To determine if sine structures are physically reasonable, we calculated the maximum value of the ordered magnetic moment, $\max(\mu_{\text{ord}})$. For a spin-only ion, this value should not normally exceed $2S\,\mu_{\text{B}}$ $(= 5.0\,\mu_{\text{B}}$ for $Mn^{2+})$. This expectation is confirmed by the low-temperature magnetization of $Na_2Mn_3Cl_8$, which saturates to approximately $5\,\mu_{\text{B}}$ per Mn^{2+} [Fig. 3(d)]. Unfortunately, we find $\max(\mu_{\text{ord}}) \gg 5.0\mu_{\text{B}}$ for the refined sine structures: $\max(\mu_{\text{ord}}) = 6.15(7)\,\mu_{\text{B}}$ at 0.3 K and $5.40(7)\,\mu_{\text{B}}$ at 0.8 K. These values are physically unreasonable, suggesting that the correct structures of $Na_2Mn_3Cl_8$ are not single-**q** sine structures.

Circular helices are promising alternative structures, since all sites have equal magnetic moment lengths. Initially, we consider circular helices with magnetic moments in either the $\mathbf{q}_\parallel\mathbf{c}$ plane, the $\mathbf{q}_\perp\mathbf{c}$ plane, or the **ab** plane (equivalent to the $\mathbf{q}_\perp\mathbf{q}_\parallel$ plane). At both 0.3 and 0.8 K, the best fit is obtained for the **ab** helix, with slightly worse agreement for the $\mathbf{q}_\perp\mathbf{c}$ helix [Table II]. The $\mathbf{q}_\parallel\mathbf{c}$ helix yields much worse agreement than the other structures, so we do not consider it further. The fits for **ab** helices at 0.3 and 0.8 K are shown in Figs. 6(b) and 6(f), respectively, and the corresponding structures are shown in Figs. 6(d) and 6(h). The agreement with the data is very good, although marginally worse than for the corresponding sine structures. Importantly, however, the refined values of μ_{ord} are now physically reasonable, with a maximum value of $4.77(5)\,\mu_{\text{B}}$ at 0.3 K. This result favors the helical structures.

We tested two variations of the helical structures in an effort to improve the fit quality. First, we considered the **ab** helix and relaxed our previous assumption of parallel basis vectors, by refining a clockwise rotation $\Delta\phi$ of the basis vector at position $\mathbf{r}_3 = (\frac{1}{2}, \frac{1}{2}, \frac{1}{2})$ about the c-axis. The optimal fit is obtained for relatively small $\Delta\phi \approx 20^\circ$ at 0.3 K, and substantial $\Delta\phi \approx 90^\circ$ at 0.8 K. Second, we maintain the assumption that the basis vectors are parallel, but vary the spin plane as $\mathbf{q}_\perp(\mathbf{q}_\parallel \cos\theta + \mathbf{c} \sin\theta)$. At 0.3 K, a minimum in R_{wp} occurs for $\theta \approx 35^\circ$, whereas at 0.8 K, fit quality is essentially unchanged for all $\theta \lesssim 30^\circ$. Each of these variations yields a similar or slightly improved fit compared to the simple **ab** helix (see Table II).

Figure 7 shows the temperature evolution of the refined parameter values for the **ab** helix with collinear basis vectors. A discontinuity in the propagation vector is apparent at T_{N2} [Fig. 7(a)]. No such anomaly is apparent in the refined value of the ordered magnetic moment, which increases smoothly on cooling the sample below T_{N1} [Fig. 7(b)]. The temperature dependence of this order parameter at low temperatures ($T \leqslant 1.2$ K) is consistent with the phenomenological form $\mu_{\text{ord}} \propto 1 - cT^2$ for a three-dimensional magnet with half-integer spin [46]. Its temperature dependence for $1.2 \leqslant T \leqslant 1.6$ K is consistent with the critical form for a three-dimensional Heisenberg magnet, $\mu_{\text{ord}} \propto (T_{N1} - T)^{0.365}$, although the small number of data points precludes fitting the critical exponent.

In conclusion, our powder-diffraction data are well explained by circular helical magnetic structures. Basis vectors are close to the **ab** plane and nearly collinear at 0.3 K, with a possibility of greater noncollinearity at 0.8 K. We emphasize, however, that the possibility of multi-**q** structures cannot be ruled out, and we discuss this further in Sec. IV B.

E. Magnetic interactions from diffuse scattering

We seek to parametrize the spin Hamiltonian of $Na_2Mn_3Cl_8$ by analyzing the diffuse magnetic scattering measured above T_{N1}. This approach is an alternative to a spin-wave analysis of inelastic neutron-scattering data and has recently been applied to several frustrated antiferromagnets [47–49]. The magnetic diffuse scattering measured at 2 and 5 K (with 40 K data subtracted) is shown in Fig. 8. Diffuse magnetic peaks are sharper at 2 K than at 5 K, consistent with an increase in the magnetic correlation length on cooling the sample. The bulk magnetic susceptibility expressed as

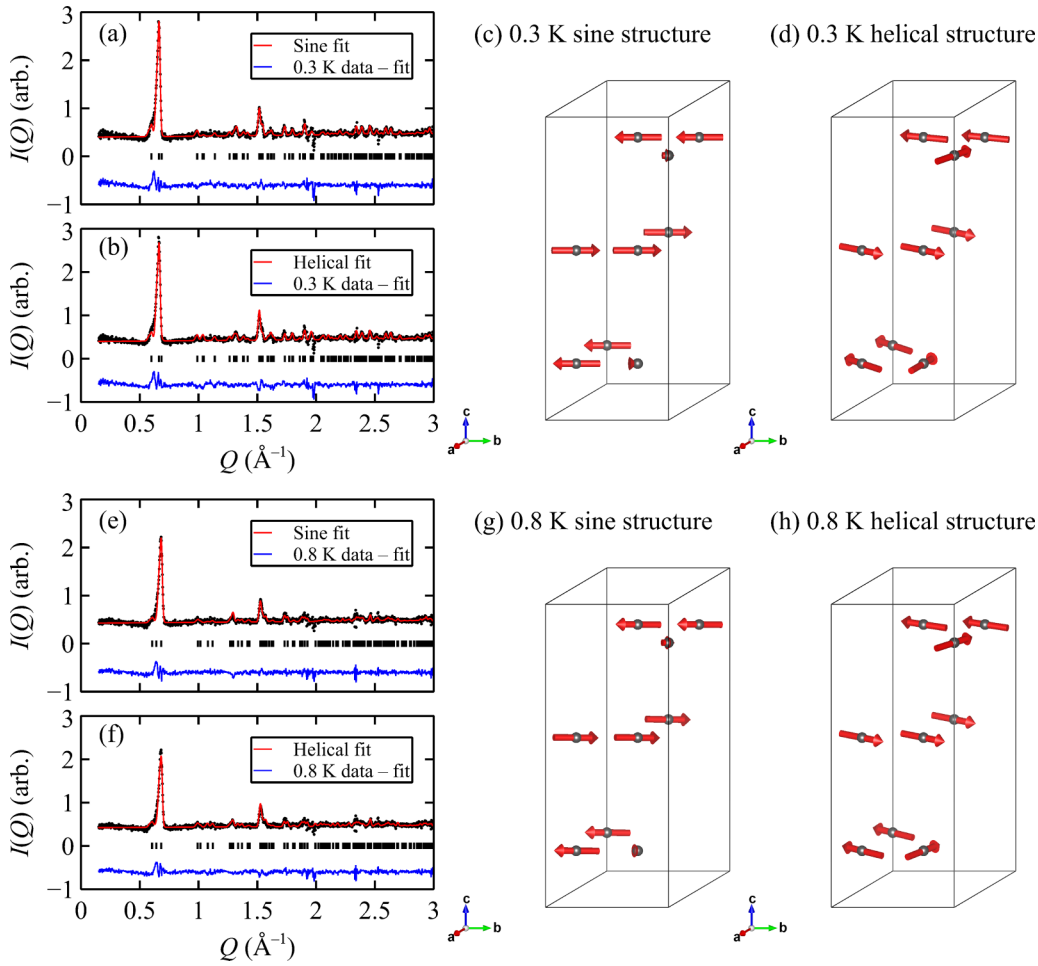

FIG. 6. [(a) and (b)] Magnetic neutron-diffraction data at $T = 0.3$ K with 2 K data subtracted (black circles), Rietveld fits for the sine (a) and helical (b) structures (red lines), and data-fit curves (blue lines). [(c) and (d)] Possible single-**q** magnetic structures at $T = 0.3$ K, showing sine (c) and helical (d) candidates. [(e) and (f)] Magnetic neutron diffraction data at $T = 0.8$ K with 2 K data subtracted (black circles), Rietveld fits for the sine (e) and helical (f) structures (red lines), and data-fit curves (blue lines). [(g) and (h)] Possible single-**q** magnetic structures at $T = 0.8$ K, showing sine (g) and helical (h) candidates.

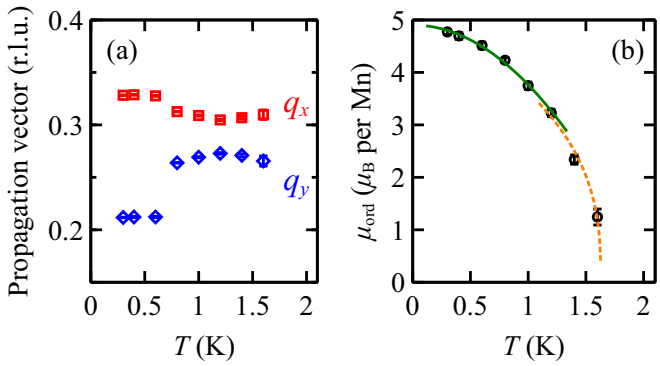

FIG. 7. Temperature dependence of refined parameters for the **ab** helix structure with collinear basis vectors. (a) Temperature evolution of the magnetic propagation vector $(q_x, q_y, \frac{3}{2})$, showing q_x (red squares) and q_y (blue diamonds). (b) Temperature evolution of the ordered magnetic moment μ_{ord} (black circles). The solid green line is a fit to $\mu_{sat}(1 - cT^2)$, where $\mu_{sat} = 4.90(4)$ μ_B and $c = 0.23(1)$ K^{-2}. The dotted orange line is a fit to the critical form for a three-dimensional Heisenberg magnet, $m(T_{N1} - T)^{0.365}$, where $T_{N1} = 1.63(1)$ K and $m = 4.3(1)$ μ_B.

χT is also shown in Fig. 8 and confirms the development of antiferromagnetic correlations. To model these data, we consider a Hamiltonian that includes Heisenberg exchange interactions and the long-range magnetic dipolar interaction,

$$H = -\sum_{i>j} J_{ij}\mathbf{S}_i \cdot \mathbf{S}_j + D\sum_{i>j} \frac{\mathbf{S}_i \cdot \mathbf{S}_j - 3(\mathbf{S}_i \cdot \hat{\mathbf{r}}_{ij})(\mathbf{S}_j \cdot \hat{\mathbf{r}}_{ij})}{(r_{ij}/r_1)^3}, \tag{4}$$

where $\mathbf{S}_i$ is modeled as a classical vector of magnitude $\sqrt{S(S+1)}$, $S = 5/2$ is the spin quantum number of Mn^{2+}, $\hat{\mathbf{r}}_{ij} = |\mathbf{r}_j - \mathbf{r}_i|/r_{ij}$ is a unit vector parallel to the separation of spins i and j, and $r_1 = 3.7124(1)$ Å is the nearest-neighbor distance. The exchange interactions include the nearest-neighbor exchange J_1, the interlayer coupling J_c, and the further-neighbor couplings shown in Fig. 1(c), so that $J_{ij} \in \{J_1, J_2, J_{3a}, J_{3b}, J_c\}$. The magnitude of the dipolar interaction at the nearest-neighbor distance, $D = \mu_0(g\mu_B)^2/4\pi r_1^3 k_B = 0.0487$ K, is determined by the crystal structure. The values of the exchange interactions were optimized against our $I(Q)$ and χT data (see Methods).

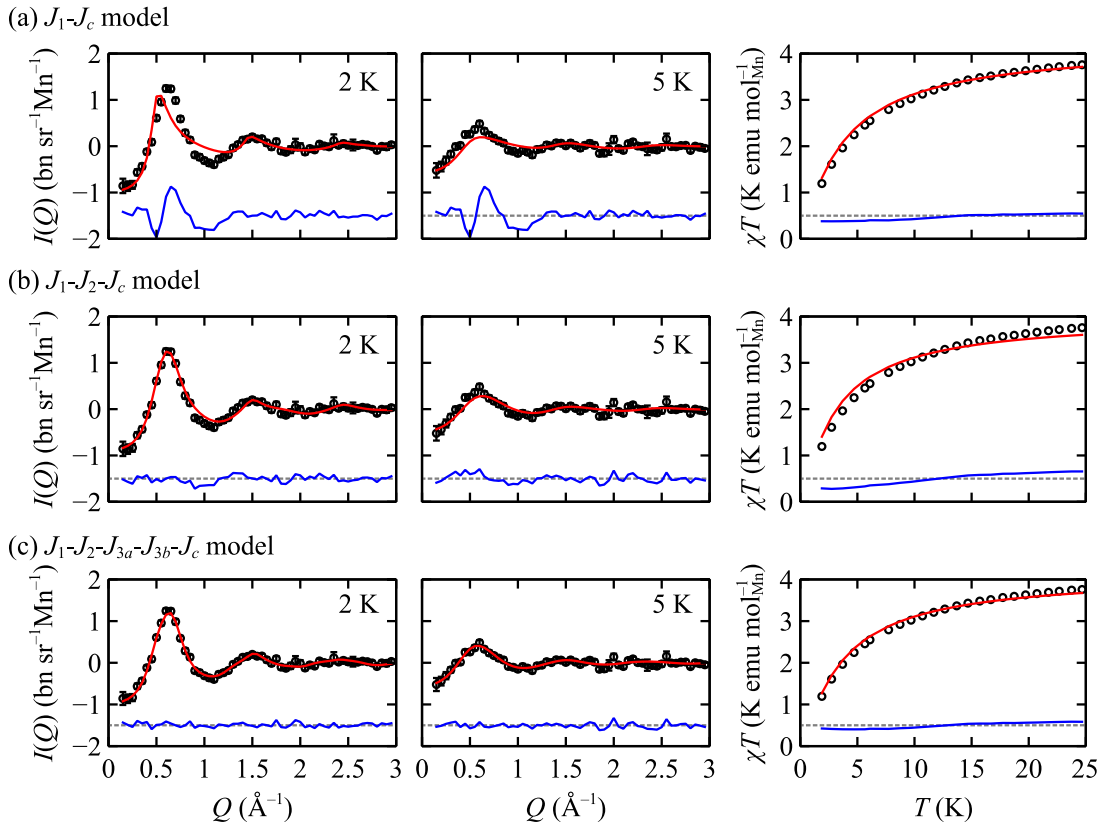

FIG. 8. Experimental data (black circles), model fits (red lines), and difference (data − fit) curves (blue lines) at temperatures above T_{N1}. Left and center columns show neutron-scattering data collected at 2 K and 5 K, respectively, and the right column shows magnetic susceptibility (χT) data. A high-temperature (40 K) data set has been subtracted from the neutron data shown. The models (a)–(c) are described in the main text, and the parameter values for each fit are given in Table III.

We tested interaction models against our data in order of increasing number of exchange parameters, as follows. Unless otherwise noted, the dipolar interaction was fixed at $D = 0.0487$ K. For each exchange model, the best fit to $I(Q)$ and χT data is shown in Fig. 8. The refined values of the exchange interactions are shown in Table III, along with the goodness of fit metric $R_{\rm wp}$, and two quantities estimated from the Onsager-reaction-field calculation that may indicate model quality: the predicted magnetic ordering temperature $T_N^{\rm calc}$ and the predicted magnetic propagation vector $\mathbf{q}_{\rm calc}$.

First, we considered a minimal model in which only J_1 and J_c were refined [model (a)]. This model does not represent our neutron data well [Fig. 8(a)], and the predicted propagation vector is commensurate, in contrast to the incommensurate propagation vector observed experimentally. Second, we refined J_1, J_2, and J_c parameters [model (b)]. This model yields a substantially improved fit, but some misfit is still evident in the $I(Q)$ and, especially, the χT data [Fig. 8(b)]. The calculated propagation vector is now incommensurate, but different to the experimental one. Third, we refined J_1, J_2, J_{3a}, J_{3b}, and J_c parameters [model (c)]. This model yields an excellent fit to both the $I(Q)$ and χT data [Fig. 8(c)]. Moreover, the calculated propagation vector, $(0.30, 0.30, \frac{3}{2})$, is close to the experimental value of $(0.3102(4), 0.2646(4), \frac{3}{2})$ in the first ordered state at 0.8 K, and the calculated $T_N^{\rm calc} \approx 1.6$ K agrees with the measured value. This refinement was stable despite the relatively large number of free parameters; no large parameter covariances ($\sigma_{ij} \geqslant 80\%$) were noted, and initializing the refinement with different parameter values yielded only

TABLE III. Refined values of interaction parameters for different models. Interaction parameter values are in K, and assume spins of magnitude $\sqrt{S(S+1)}$ with $S = 5/2$ for Mn^{2+}. Positive values indicate ferromagnetic interactions. Parameter values held fixed are indicated with an asterisk (*).

	J_1 (K)	J_2 (K)	J_{3a} (K)	J_{3b} (K)	J_c (K)	D (K)	$R_{\rm wp}^{\rm neutron}$	$R_{\rm wp}^{\chi \rm T}$	$\mathbf{q}_{\rm calc}$	$T_N^{\rm calc}$ (K)
(a)	−0.060(3)	0*	0*	0*	−0.247(4)	0.0487*	53.0	2.3	$(0, 0, \frac{3}{2})$	1.63
(b)	0.009(5)	−0.073(4)	0*	0*	−0.196(6)	0.0487*	28.0	4.2	(0.56, −0.56, 0.56)	1.36
(c)	0.09(1)	0.02(1)	−0.28(1)	−0.12(2)	−0.06(2)	0.0487*	19.2	2.2	$(0.30, 0.30, \frac{3}{2})$	1.57
(d)	0.16(1)	0.04(1)	−0.30(1)	−0.13(3)	−0.08(1)	0*	25.3	2.0	$(0.28, 0.28, \frac{3}{2})$	1.00

one possible local minimum, which had significantly worse $R_{\rm wp}^{\rm neutron} = 23.0\%$ and $R_{\rm wp}^{\chi T} = 4.1\%$.

Our results suggest that model (c) represents well the interactions of $Na_2Mn_3Cl_8$. This model has weak ferromagnetic J_1, consistent with the Goodenough-Kanamori rules. The interlayer coupling J_c is antiferromagnetic, consistent with the antiferromagnetic layer stacking observed below T_{N1}. The third-neighbor couplings J_{3a} and J_{3b} are antiferromagnetic and significantly larger than J_1. Hence, $Na_2Mn_3Cl_8$ is an unusual system where strong antiferromagnetic third-neighbor interactions compete with ferromagnetic nearest-neighbor interactions. To the best of our knowledge, a similar J_1-J_3 competition has been identified in only one other kagome material, vesignieite [50]. However, this material differs from $Na_2Mn_3Cl_8$ in its magnetic properties as well as its chemistry, as it has $S = 1/2$ and shows commensurate magnetic ordering [50].

Finally, we considered the relevance of the long-ranged dipolar interaction by performing a fourth refinement in which J_1, J_2, J_{3a}, J_{3b}, and J_c parameters were varied, while D was fixed at zero [model (d)]. This refinement yielded worse agreement with $I(Q)$ and χT data, and significantly underestimates the value of T_{N1} (Table III). This result shows that the dipolar interaction has a significant effect on the magnetic properties, as expected since D is of comparable magnitude to the exchange interactions. However, the refined values of all parameters except J_1 are equivalent (within 1σ) for models (c) and (d), suggesting that the effect of the dipolar term on these refinements is largely confined to nearest neighbors.

IV. THEORY AND MODELING

A. Magnetic interactions from first principles

To gain insight into the exchange interactions, we performed first-principles calculations using density-functional theory (see Methods). The values of the interactions calculated using DFT are given in Table IV for different values of the Hubbard U between 0 and 5.25 eV. Based on other materials, we anticipate that U is likely between 4 and 5.25 eV.

The first-principles exchange interactions show similarities with the experimentally determined values, but also substantial differences. On the one hand, the first-principles values of J_1 and J_c are ferromagnetic and antiferromagnetic, respectively, consistent with the values fitted to experimental data. The magnitudes of J_1 and J_c for $U = 5.25$ eV are also comparable to the experimentally determined magnitudes, in contrast to a previous DFT study that reported interactions larger than 30 K [20]. On the other hand, the first-principles values of J_2, J_{3a}, and J_{3b} are *opposite* to the experimentally determined values; moreover, the calculated magnitudes of these interactions are very large compared to the other interactions.

TABLE IV. Values of interaction parameters obtained from density-functional theory simulations for different values of the Hubbard U.

U (eV)	J_1 (K)	J_2 (K)	J_{3a} (K)	J_{3b} (K)	J_c (K)
0	0.516	−1.321	0.801	1.045	−0.040
2.00	0.288	−0.745	0.525	0.591	−0.029
4.00	0.194	−0.507	0.411	0.406	−0.024
5.25	0.163	−0.430	0.377	0.346	−0.023

We carefully checked whether the first-principles results could be consistent with our experimental data. Taking $U = 5.25$ eV, we calculate the Weiss temperature as $\theta_{\rm DFT} = \frac{4}{3}S(S+1)[J_1 + J_2 + J_c + J_{3a} + J_{3b}/2] = 3.0$ K. Hence, DFT predicts a ferromagnetic Weiss temperature, which is not consistent with the antiferromagnetic value [$\theta = -4.6(1)$ K] measured experimentally. We also estimate the magnetic ordering temperature to be 4.8 K, which is much larger than the experimental value of 1.6 K. Finally, we performed additional refinements to neutron and χT data as described in Sec. III E, except we constrained the signs of the exchange interactions to be the same as those from DFT, while allowing their magnitudes to refine freely. These refinements yielded $J_{3a} = J_{3b} \approx 0$, essentially reproducing the results of model (b) in Sec. III E.

We therefore conclude that the DFT results are not fully consistent with our experimental data, making $Na_2Mn_3Cl_8$ a model material for benchmarking developments in first-principles calculations. The reason for the inaccuracy of the DFT exchange interactions beyond nearest-neighbors is not yet clear. As discussed in the Methods, we checked the effect of spin-orbit coupling, and found it to be negligible in our calculations. An interesting possibility is that the discrepancy may relate to the neglect of the Stoner coupling on the Cl ligand sites, as recently proposed in the related material $NaMnCl_3$ [51].

B. Origin of incommensurate ordering

In this section, we discuss the origin of the multiple incommensurate ordering transitions in $Na_2Mn_3Cl_8$, using a combination of field-theoretic and Monte Carlo simulations.

Incommensurate magnetic structures are relatively uncommon in kagome antiferromagnets. For example, to the best of our knowledge, all known jarosite minerals that exhibit long-range order have either (0,0,0) or $(0, 0, \frac{3}{2})$ propagation vectors (see Ref. [52] and references therein). Similarly, commensurate states are observed for many other insulating materials in which the kagome lattice is undistorted or slightly distorted; for example, $MgFe_3(OH)_6Cl_2$ with $\mathbf{q} = (0, 0, \frac{3}{2})$ [53], centennialite $CaCu_3(OH)_6Cl_2 \cdot 0.6H_2O$ [54], $CdCu_3(OH)_6(NO_3)_2 \cdot 0.6H_2O$ [55], $Nd_3Sb_3Mg_2O_{14}$ [56], and Sr-vesignieite $SrCu_3V_2O_8(OH)_2$ with $\mathbf{q} = (0, 0, 0)$, α-$Cu_3Mg(OH)_6Br_2$ [57] and $YCu_3(OH)_6Cl_3$ with $\mathbf{q} = (0, 0, \frac{1}{2})$ [58], and Ba-vesignieite $BaCu_3V_2O_8(OH)_2$ with $\mathbf{q} = (\frac{1}{2}, 0, 0)$ [50,59]. By contrast, the distorted-kagome material $Ba_2Mn_3F_{11}$ is one of the only insulating kagome materials with incommensurate magnetic ordering [60]. Incommensurate modulations are more frequently observed in metallic kagome systems, such as $Tb_3Ru_4Al_{12}$ [61] and YMn_6Sn_6, the latter of which undergoes a commensurate-to-incommensurate transition on cooling [62].

To understand the preference for kagome magnets to form commensurate structures, and the conditions where incommensurate structures may appear, we use the reciprocal-space mean-field approximation introduced in Sec. II C to investigate the stability of different phases as a function of the interactions J_1, J_{3a}, J_{3b}, and J_c [Fig. 1(c)]. Throughout large

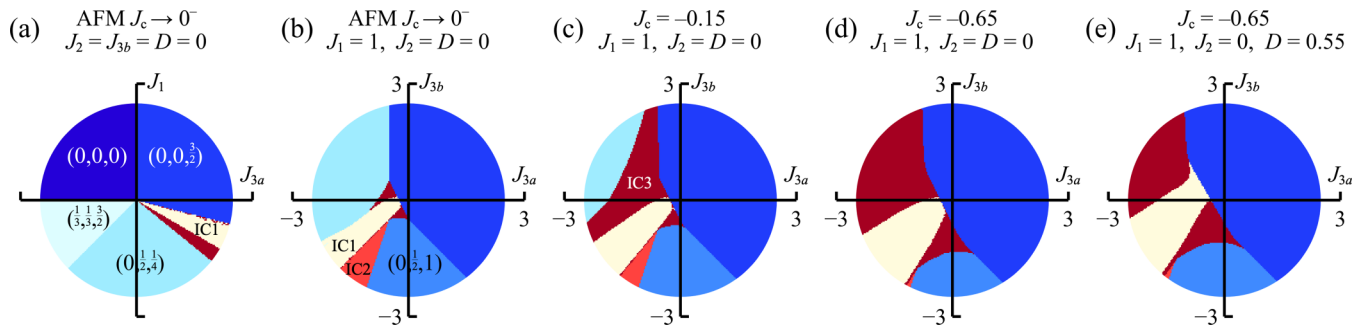

FIG. 9. Mean-field phase diagrams for the kagome lattice of $Na_2Mn_3Cl_8$. The values of fixed interaction parameters are given above each phase diagram (a)–(e), and axes are labeled with the variable interaction parameters. Different magnetic propagation vectors $\mathbf{q}$ are indicated by different colors, with the $\mathbf{q}$ corresponding to each color labeled in the leftmost phase diagram in which it occupies a wide phase space. The propagation vectors include (0,0,0), $(0, 0, \frac{3}{2})$, $(\frac{1}{3}, \frac{1}{3}, \frac{3}{2})$, $(0, \frac{1}{2}, \frac{1}{4})$, $(0, \frac{1}{2}, 1)$, and three incommensurate vectors, IC1 $= (q, q, \frac{3}{2})$, IC2 $= (q, q, 0)$, and IC2 $= (0, q, r)$. Note that the interlayer coupling J_c is antiferromagnetic for all phase diagrams, and the nearest-neighbor coupling J_1 is ferromagnetic for (b)–(e).

regions of this interaction space, the classical ground state is one of the commensurate "regular magnetic orders" described in Ref. [15]. Of the models previously investigated theoretically, the most relevant one to $Na_2Mn_3Cl_8$ is the J_1-J_{3a} Heisenberg model studied in Refs. [16,17]. The phase diagram for this model is shown in Fig. 9(a), and contains five phases: ferromagnetic layers with antiferromagnetic stacking [$\mathbf{q} = (0, 0, \frac{3}{2})$], $\mathbf{q} = \mathbf{0}$ antiferromagnet, $\sqrt{3}\times\sqrt{3}$ antiferromagnet [$\mathbf{q} = (\frac{1}{3}, \frac{1}{3}, \frac{3}{2})$], three-sublattice antiferromagnet [$\mathbf{q} = (0, \frac{1}{2}, \frac{1}{4})$], and an incommensurate region. This result reproduces the result of Ref. [16] for isolated kagome planes, except that we include a small antiferromagnetic interlayer coupling $J_c \to 0^-$ to stabilize three-dimensional ordering.

While the J_1-J_{3a} phase diagram is relatively complicated, it is nevertheless simpler than our model for $Na_2Mn_3Cl_8$, which also includes significant J_c, J_{3b}, and dipolar couplings. We therefore extended the J_1-J_{3a} phase diagram to consider the effects of these additional couplings, which are needed for a full description of our $Na_2Mn_3Cl_8$ data. Notably, for all models, antiferromagnetic J_{3a} is necessary to stabilize incommensurate ordering with $\mathbf{q} = (q, q, \frac{3}{2})$. In Fig. 9(b), we fix ferromagnetic $J_1 = 1$ and consider the phase diagram in the J_{3a}-J_{3b} plane for antiferromagnetic $J_c \to 0^-$. Nonzero J_{3b} has a dramatic effect on the phase diagram; in particular, including antiferromagnetic J_{3b} extends the stability region of the incommensurate phases observed for antiferromagnetic J_{3a}. Figures 9(b)–9(d) show the effect of increasing the magnitude of J_c, the antiferromagnetic interlayer coupling ($J_c \to 0^-$, -0.15, and -0.65, respectively, in the same units as J_1). The effect of increasing $|J_c|$ is to increase further the region of phase space in which incommensurate order is stable within the mean-field approximation. Finally, in Fig. 9(e), we show the J_{3a}-J_{3b} phase diagram including the long-range dipolar interaction $D/J_1 \approx 0.55$ appropriate for $Na_2Mn_3Cl_8$. The inclusion of D has a relatively small effect on the positions of the phase boundaries.

The reciprocal-space mean-field theory provides a useful overview of the phase space, but has several important limitations. First, for a non-Bravais lattice such as kagome, it only determines a lower bound on the energy of the ground state. As discussed in Ref. [16], for the incommensurate region of the J_1-J_{3a} phase diagram, a physical spin configuration could not be identified that reached this lower bound; hence, the actual magnetic ground state is uncertain in this region. Second, since this theory considers instabilities of the paramagnetic phase, it predicts only the propagation vector of the first ordered state that develops on cooling; it provides no information about the possibility of multiple phase transitions, as are observed experimentally in $Na_2Mn_3Cl_8$.

We performed classical Monte Carlo simulations to address these limitations. Since the periodicity of an incommensurate magnetic structure does not "fit" within any finite-sized configuration, finite-size artifacts are encountered, which can be reduced by studying relatively large system sizes. However, the long-ranged nature of the magnetic dipolar interaction makes large system sizes computationally expensive. We therefore consider first an approximation to the full Hamiltonian, Eq. (4), where we simulate the parameters that best describe our diffuse-scattering data [model (c) in Table III], but truncate the dipolar interaction D at the nearest-neighbor distance; we will call this the "nearest-neighbor dipolar model." For comparison, we also simulated the same model (c) except with $D = 0$. To identify finite-size effects, we considered different system dimensions from $10\times10\times4$ hexagonal unit cells (3600 spins) to $20\times20\times8$ hexagonal unit cells (28800 spins). For the $10\times10\times4$ and $20\times20\times8$ simulations only, we slightly adjusted the model (c) interaction parameters to stabilize $\mathbf{q} = (\frac{3}{10}, \frac{3}{10}, \frac{3}{2})$ ordering, which is commensurate with the system size; this was achieved by multiplying the best-fit values of J_{3a} and J_{3b} by 0.936. To investigate the effect of a different system geometry, we defined a orthogonal unit cell with axes $\mathbf{a}_o = \mathbf{a}$, $\mathbf{b}_o = \mathbf{a} + 2\mathbf{b}$, and $\mathbf{c}_o = \mathbf{c}$, and performed simulations of $12\times6\times4$ and $18\times9\times6$ orthogonal unit cells (5184 and 17 496 spins, respectively). Simulations were run for up to 4.1×10^6 moves per spin at low temperatures, where a single move involved one microcanonical (over-relaxation) update followed by a proposed spin rotation of a randomly chosen spin, which was accepted or rejected according to the Metropolis criterion. Measurements of the autocorrelation function showed that these conditions allowed the system to decorrelate at all temperatures above 0.1 K. Simulations including the long-ranged dipolar inter-

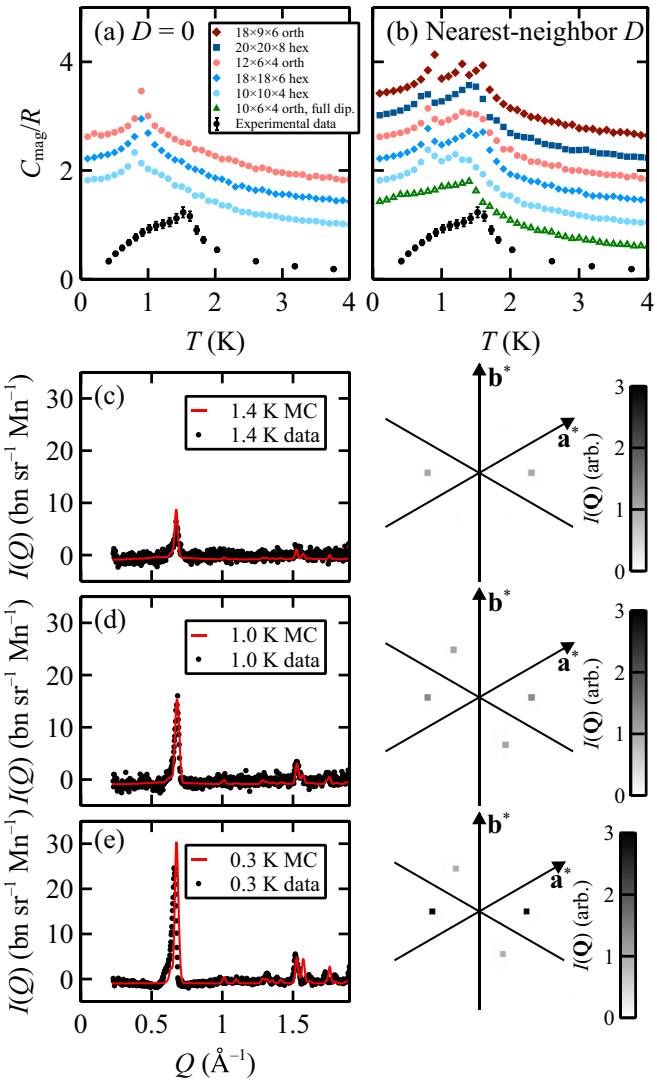

FIG. 10. (a) Magnetic specific heat calculated from Monte Carlo simulations of the exchange parameters of model (c) in Table III, taking the dipolar interaction $D = 0$. Experimental data are also shown for comparison. Successive curves are vertically offset by 0.4 units for clarity. (b) As (a), except the dipolar interaction is included, either for all neighbors (green triangles) or for nearest neighbors only (all other points). The simulated system sizes are as shown in the key in (a). (c) Magnetic diffraction patterns at $T = 1.4$ K, showing calculated powder diffraction profile from Monte Carlo simulation (red line, left), experimental powder-diffraction data (black circles, left), and calculated single-crystal diffraction pattern from Monte Carlo simulation (grayscale plot, right). (d) As (c), except at $T = 1.0$ K. (e) As (c), except at $T = 0.3$ K.

action, implemented using Ewald summation [63], were also performed for a small system size of 10×6×4 orthogonal unit cells, without over-relaxation updates.

Results of our Monte Carlo simulations are compared with our experimental data in Fig. 10. For the model with $D = 0$, a sharp specific-heat anomaly indicating a single magnetic phase transition is observed at ≈0.9 K [Fig. 10(a)]; we do not consider the low-temperature state here. The nearest-neighbor dipolar model shows a more complex temperature evolution [Fig. 10(b)]. In all our simulations, sharp specific heat anomaly is observed at ≈0.9 K, with a second feature between 1.3 and 1.6 K that is resolved as either a single broadened peak or two peaks close in temperature, depending on system dimensions. Hence, unlike the Heisenberg model, the nearest-neighbor dipolar model shows at least two magnetic phase transitions, in qualitative agreement with the experimental data for $Na_2Mn_3Cl_8$. Properties of the magnetic phases obtained for a model of 18×9×6 orthogonal unit cells are shown at 1.4, 1.0, and 0.3 K, in Fig. 10(c)–10(e) respectively. The phases observed at 1.0 and 0.3 K are resolved for all other system sizes and geometries. However, the 1.4 K phase is not resolved in the 20×20×8 simulation, suggesting its appearance for some other system sizes may be a finite-size artifact. The calculated magnetic powder diffraction patterns show remarkably good agreement with our experimental powder-diffraction data, especially at 1.4 and 1.0 K [Figs. 10(c)–10(e)]. Calculations of the single-crystal magnetic diffraction patterns reveal magnetic Bragg peaks corresponding to a single incommensurate wave vector at 1.4 K, indicating a single-**q** magnetic structure at this temperature [Fig. 10(c)]. Remarkably, however, the same calculation shows magnetic Bragg peaks corresponding to two wave vectors at 1.0 and 0.3 K. The intensity of each wave vector is approximately equal at 1.0 K but significantly different at 0.3 K [Figs. 10(d) and 10(e)]. The same effect was observed across all our simulations at 1.0 and 0.3 K, suggesting this is likely not an artifact due to domain formation, but instead indicates the formation of double-**q** states in the Monte Carlo simulations. Our simulations of the long-ranged dipolar model also suggest possible changes in magnetic structure below approximately 1.0 K, although further transitions are not clearly resolved in the heat capacity for this small simulation size [Fig. 10(b)]. For this model, the magnetic structure is clearly 2-**q** only below 1.0 K.

Our results suggest the enticing possibility that the ordered incommensurate states may, in fact, be multi-**q** structures rather than single-**q** helices. Given the good agreement of our microscopic model with powder-diffraction data and its correct prediction of multiple phase transitions, this scenario is certainly possible. Further theoretical studies including the long-ranged dipolar interaction would be useful to elucidate the relative stabilities of single-**q** and multi-**q** states, which may be close in energy.

V. CONCLUSIONS

Our neutron-diffraction study reveals that $Na_2Mn_3Cl_8$ shows novel magnetic behavior. Unusually for a kagome antiferromagnet, it shows incommensurate ordering; even more unusually, it exhibits multiple incommensurate magnetic phases, which form at 1.6 and 0.6 K. To the best of our knowledge, ordering wave vectors of the form $(q_x, q_y, \frac{3}{2})$, as observed in $Na_2Mn_3Cl_8$, have not previously been observed in insulating kagome magnets. As such, $Na_2Mn_3Cl_8$ significantly expands the known range of magnetic behavior on the kagome lattice.

We investigated the magnetic interactions that drive incommensurate ordering in $Na_2Mn_3Cl_8$ using experiment-driven and first-principles approaches. By fitting the magnetic diffuse scattering measured above the magnetic ordering temperature,

we showed that the magnetic interactions extend to third-nearest neighbors. Antiferromagnetic third-neighbor interactions J_{3a} and J_{3b} are the largest terms in the Hamiltonian, and compete with ferromagnetic nearest-neighbor interactions J_1. Using a mean-field theory, we showed that antiferromagnetic J_{3a}, J_{3b}, and interlayer couplings extends the stability region of incommensurate ordering in a model with ferromagnetic J_1. Our experimentally determined interactions could not be fully reproduced by DFT calculations, which predict ferromagnetic J_{3a} and J_{3b}, inconsistent with our experimental data. This material may therefore be a useful test case for advancements in first-principles methodologies.

Using magnetic Rietveld refinement, we showed that the magnetic Bragg profiles of the two incommensurate magnetic phases are well described by single-**q** helical structures. These are cycloidal helices, in which the spins and the propagation vector **q** both have a component in the *ab* plane. Due to the limitations of powder data, however, other structures can give equivalent or slightly better agreement with the experimental pattern. We showed that single-**q** sine structures are highly unlikely at 0.8 and 0.3 K, since some sites would have unphysically large magnitudes of the ordered magnetic moment. However, we were not able to rule out multi-**q** structures, which are generally indistinguishable from their single-**q** analogs in powder diffraction measurements. This issue is especially relevant here, because Monte Carlo simulations of our experimentally determined interaction model show multiple magnetic phases transitions, in qualitative agreement with the experimental data, and indicate that two of the phases obtained are 2-**q** states. Further experiments would therefore be valuable to distinguish between single-**q** and double-**q** states. These experiments could include single-crystal neutron diffraction under applied magnetic field, or inelastic neutron scattering. The growth of large single crystals of $Na_2Mn_3Cl_8$ would facilitate such measurements and potentially shed further light on the nature of the spin texture in $Na_2Mn_3Cl_8$.

ACKNOWLEDGMENTS

We are grateful to Andrew Christianson (ORNL) and Brenden Ortiz (ORNL) for valuable discussions. This work was supported by the U.S. Department of Energy (DOE), Office of Science, Basic Energy Sciences, Materials Sciences and Engineering Division, and used resources at the High Flux Isotope Reactor, a DOE Office of Science User Facility operated by the Oak Ridge National Laboratory.

[1] L. Balents, Nature (London) **464**, 199 (2010).
[2] J. T. Chalker, P. C. W. Holdsworth, and E. F. Shender, Phys. Rev. Lett. **68**, 855 (1992).
[3] M. E. Zhitomirsky, Phys. Rev. B **78**, 094423 (2008).
[4] M. R. Norman, Rev. Mod. Phys. **88**, 041002 (2016).
[5] M. A. de Vries, J. R. Stewart, P. P. Deen, J. O. Piatek, G. J. Nilsen, H. M. Rønnow, and A. Harrison, Phys. Rev. Lett. **103**, 237201 (2009).
[6] T.-H. Han, J. S. Helton, S. Chu, D. G. Nocera, J. A. Rodriguez-Rivera, C. Broholm, and Y. S. Lee, Nature (London) **492**, 406 (2012).
[7] T.-H. Han, J. Singleton, and J. A. Schlueter, Phys. Rev. Lett. **113**, 227203 (2014).
[8] C. M. Pasco, B. A. Trump, T. T. Tran, Z. A. Kelly, C. Hoffmann, I. Heinmaa, R. Stern, and T. M. McQueen, Phys. Rev. Mater. **2**, 044406 (2018).
[9] K. Tustain, G. J. Nilsen, C. Ritter, I. da Silva, and L. Clark, Phys. Rev. Mater. **2**, 111405(R) (2018).
[10] A. S. Wills and A. Harrison, J. Chem. Soc. Faraday Trans. **92**, 2161 (1996).
[11] T. Inami, M. Nishiyama, S. Maegawa, and Y. Oka, Phys. Rev. B **61**, 12181 (2000).
[12] M. Nishiyama, S. Maegawa, T. Inami, and Y. Oka, Phys. Rev. B **67**, 224435 (2003).
[13] S. Janas, M. B. Sørensen, A. B. A. Andersen, M. Juelsholt, M. Boehm, K. S. Pedersen, K. M. Ø. Jensen, K. Lefmann, and U. G. Nielsen, Phys. Chem. Chem. Phys. **22**, 25001 (2020).
[14] W. G. Bisson and A. S. Wills, J. Phys.: Condens. Matter **20**, 452204 (2008).
[15] L. Messio, C. Lhuillier, and G. Misguich, Phys. Rev. B **83**, 184401 (2011).
[16] V. Grison, P. Viot, B. Bernu, and L. Messio, Phys. Rev. B **102**, 214424 (2020).
[17] H. Li and T. Li, Phys. Rev. B **106**, 035112 (2022).
[18] C. J. J. Loon and D. J. W. Ijdo, Acta Cryst. B **31**, 770 (1975).
[19] K. P. Devlin and R. Cava, Solid State Commun. **342**, 114598 (2022).
[20] V. Meschke, P. Gorai, V. Stevanović, and E. S. Toberer, Chem. Mater. **33**, 4373 (2021).
[21] D. J. Hinz, G. Meyer, T. Dedecke, and W. Urland, Angew. Chem. Int. Ed. Engl. **34**, 71 (1995).
[22] N. Hänni, M. Frontzek, J. Hauser, D. Cheptiakov, and K. Krämer, Z. Anorg. Allg. Chem. **643**, 2063 (2017).
[23] Z. A. Kelly, T. T. Tran, and T. M. McQueen, Inorg. Chem. **58**, 11941 (2019).
[24] A. Paul, C.-M. Chung, T. Birol, and H. J. Changlani, Phys. Rev. Lett. **124**, 167203 (2020).
[25] D. I. Khomskii, T. Mizokawa, and S. V. Streltsov, Phys. Rev. Lett. **127**, 049701 (2021).
[26] A. W. Hewat, Acta Cryst. A **35**, 248 (1979).
[27] J. A. M. Paddison, arXiv:2210.09016.
[28] D. E. Logan, Y. H. Szczech, and M. A. Tusch, Europhys. Lett. **30**, 307 (1995).
[29] R. Brout and H. Thomas, Phys. Phys. Fiz. **3**, 317 (1967).
[30] M. Enjalran and M. J. P. Gingras, Phys. Rev. B **70**, 174426 (2004).
[31] F. James and M. Roos, Comput. Phys. Commun. **10**, 343 (1975).
[32] F. James, MINUIT Function Minimization and Error Analysis: Reference Manual Version 94.1, CERN (1994).
[33] J. Rodriguez-Carvajal, An Introduction to the Program FullProf 2000, CEA-CRNS, France (2000).
[34] J. Rodríguez-Carvajal, Phys. B: Condens. Matter **192**, 55 (1993).
[35] K. Momma and F. Izumi, J. Appl. Cryst. **41**, 653 (2008).
[36] E. Sjöstedt, L. Nordström, and D. Singh, Solid State Commun. **114**, 15 (2000).
[37] P. Blaha, K. Schwarz, G. K. H. Madsen, D. Kvasnicka, and J. Luitz, *WIEN2K, an Augmented Plane Wave+Local Orbitals*

Program for Calculating Crystal Properties (Technische Universität Wien, Vienna, 2001).
[38] D. J. Singh and L. Nordstrom, *Planewaves Pseudopotentials and the LAPW Method* (Springer, Berlin, 2006).
[39] J. P. Perdew, K. Burke, and M. Ernzerhof, Phys. Rev. Lett. **77**, 3865 (1996).
[40] K. Yamauchi, F. Freimuth, S. Blügel, and S. Picozzi, Phys. Rev. B **78**, 014403 (2008).
[41] N. S. Fedorova, C. Ederer, N. A. Spaldin, and A. Scaramucci, Phys. Rev. B **91**, 165122 (2015).
[42] X. Liu, J. Ping Liu, Q. Zhang, and Z. Altounian, Phys. Lett. A **377**, 731 (2013).
[43] H. Nakano and T. Sakai, J. Phys. Soc. Jpn. **84**, 063705 (2015).
[44] A. Wills, Physica B: Condens. Matter **276–278**, 680 (2000).
[45] J. S. Kouvel and J. S. Kasper, J. Phys. Chem. Solids **24**, 529 (1963).
[46] U. Köbler, A. Hoser, and D. Hupfeld, Physica B: Condens. Matter **328**, 276 (2003).
[47] A. M. Samarakoon, Y. W. Li, M. Eisenbach, Q. Zhang, F. Ye, V. Sharma, Z. L. Dun, H. Zhou, S. A. Grigera, C. D. Batista *et al.*, Nat. Commun. **11**, 892 (2020).
[48] A. O. Scheie, J. Xing, J. A. M. Paddison, N. E. Sherman, M. Dupont, L. D. Sanjeewa, S. Lee, A. J. Woods, D. Abernathy, D. M. Pajerowski *et al.*, arXiv:2109.11527.
[49] P. G. Welch, J. A. M. Paddison, M. D. Le, J. S. Gardner, W.-T. Chen, A. R. Wildes, A. L. Goodwin, and J. R. Stewart, Phys. Rev. B **105**, 094402 (2022).
[50] D. Boldrin, B. Fåk, E. Canévet, J. Ollivier, H. C. Walker, P. Manuel, D. D. Khalyavin, and A. S. Wills, Phys. Rev. Lett. **121**, 107203 (2018).
[51] I. V. Solovyev, A. V. Ushakov, and S. V. Streltsov, Phys. Rev. B **106**, L180401 (2022).
[52] P. Mendels and A. S. Wills, in *Kagomé Antiferromagnets: Materials Vs. Spin Liquid Behaviors* (Springer, Berlin, Heidelberg, 2011), pp. 207–238.
[53] M. Fujihala, X. G. Zheng, S. Lee, T. Kamiyama, A. Matsuo, K. Kindo, and T. Kawae, Phys. Rev. B **96**, 144111 (2017).
[54] K. Iida, H. K. Yoshida, A. Nakao, H. O. Jeschke, Y. Iqbal, K. Nakajima, S. Ohira-Kawamura, K. Munakata, Y. Inamura, N. Murai, M. Ishikado, R. Kumai, T. Okada, M. Oda, K. Kakurai, and M. Matsuda, Phys. Rev. B **101**, 220408(R) (2020).
[55] Y. Ihara, R. Hiyoshi, M. Shimohashi, K. Hayashi, R. Okuma, F. Orlandi, P. Manuel, G. J. Nilsen, and Z. Hiroi, Phys. Rev. B **106**, 024401 (2022).
[56] A. Scheie, M. Sanders, J. Krizan, Y. Qiu, R. J. Cava, and C. Broholm, Phys. Rev. B **93**, 180407(R) (2016).
[57] Y. Wei, Z. Feng, C. dela Cruz, W. Yi, Z. Y. Meng, J.-W. Mei, Y. Shi, and S. Li, Phys. Rev. B **100**, 155129 (2019).
[58] A. Zorko, M. Pregelj, M. Gomilšek, M. Klanjšek, O. Zaharko, W. Sun, and J.-X. Mi, Phys. Rev. B **100**, 144420 (2019).
[59] Y. Okamoto, H. Yoshida, and Z. Hiroi, J. Phys. Soc. Jpn. **78**, 033701 (2009).
[60] S. Hayashida, H. Ishikawa, Y. Okamoto, T. Okubo, Z. Hiroi, M. Avdeev, P. Manuel, M. Hagihala, M. Soda, and T. Masuda, Phys. Rev. B **97**, 054411 (2018).
[61] S. Rayaprol, A. Hoser, K. K. Iyer, S. K. Upadhyay, and E. Sampathkumaran, J. Magn. Magn. Mater. **477**, 83 (2019).
[62] N. J. Ghimire, L. Poudel, D. C. Jones, D. Michel, N. T. Magar, M. Bleuel, M. A. McGuire, J. S. Jiang, J. F. Mitchell, and J. W. Lynn *et al.*, Sci. Adv. **6**, eabe2680 (2020).
[63] Z. Wang and C. Holm, J. Chem. Phys. **115**, 6351 (2001).